

Near Infrared Emission at 1000 nm from Nanostructured Pr³⁺/Yb³⁺ Co-doped SiO₂-Nb₂O₅ for Solar Cell Application

Wesley C. Muscelli,^a Felipe T. Aquino,^a Sidney J. L. Ribeiro^b and Rogéria R. Gonçalves^{*a}

^aDepartamento de Química, Faculdade de Filosofia, Ciências e Letras de Ribeirão Preto, Universidade de São Paulo, Av. Bandeirantes, 3900, 14040-901 Ribeirão Preto-SP, Brazil

^bInstituto de Química, UNESP, 14800-900 Araraquara-SP, Brazil

Energy conversion, involving UV and Vis absorption to generate near infrared (NIR) emission at 1000 nm from nanostructured Pr³⁺/Yb³⁺ co-doped SiO₂-Nb₂O₅ for solar cell application was the main focus of this work. The synthesis, structural and optical characterization of Pr³⁺/Yb³⁺ co-doped 70SiO₂-30Nb₂O₅ nanocomposites and planar waveguides prepared by the sol gel method are reported. The influence of the rare earth content and thermal annealing on the crystallization process and the luminescence properties was studied. The excitation spectra revealed the energy transfer between the Pr³⁺ and Yb³⁺, involving mainly the ³P₂ level of Pr³⁺ ions. Multiphonon decay and cross relaxation processes take place at higher rare earth concentration and annealing temperature, which increases the ¹D₂ level population and consequently the NIR emission from the Pr³⁺ ions. The nanostructured Pr³⁺/Yb³⁺ co-doped SiO₂-Nb₂O₅ nanocomposites and waveguides show interesting NIR emission and optical properties for photonic applications.

Keywords: nearinfrared emission, energy conversion, praseodimium, ytterbium, luminescence

Introduction

Rare earth doped materials for photonic applications have been increasingly reported on literature in a huge number of applications such as light emitting,^{1,2} biomedical,³⁻⁵ telecommunications,^{6,7} solar cells,^{8,9} among others. Considering the different rare earth ions, praseodymium (Pr³⁺) shows a complex electronic structure, with many absorption bands in the UV, visible and near infrared (NIR) ranges. Therefore, Pr³⁺-doped materials have been reported for many potential applications, e.g., as optical amplifiers operating at 1.3 μm,^{10,11} not to mention the materials emitting in the blue,¹² orange,¹³ red,¹⁴ and white light,^{15,16} which enables applications like upconverter lasers and light emitting diodes (LEDs). NIR luminescence from Pr³⁺-Yb³⁺ co-doped materials have been reported, specially the luminescence of Yb³⁺ at 980 nm after resonant excitation of the ³P₁ levels of Pr³⁺.¹⁷⁻¹⁹ The single excited state ²F_{5/2} around 10.000 cm⁻¹ (1.24 eV) is close to the silicon band-gap energy (1.12 eV), and consequently is specifically interesting considering solar cells application, since Yb³⁺ emission can be efficiently absorbed without significant thermalization losses.²⁰

Among the mentioned photonic applications, the renewable energy supply technologies have attracted considerable attention in the last years due to the increasing energy demand and the concerns about reduced environmental impact in the energy production. Thus, the photovoltaic energy technologies have been gradually developed towards new technologies and new materials enabling the conversion of solar energy into electrical energy.²¹ Photovoltaic solar cells (PV) based on the silicon present many advantages such as low production cost, non-toxicity, easy of passivation and texturing.²² However, low energy conversion efficiency by the commercial silicon solar cells is the major reason of solar energy production still remains non-price competitive. According to Shockley-Queisser limit, only 32% of the solar spectrum can be used for the photoelectron generation.²³ The absorption of high energy photons can generate an electron-hole pair with lost of excess energy as heat. In addition, low energy photons, i.e., photons with energy lower than the silicon band gap are not absorbed by the solar cells.

An alternative strategy to obtain PV solar cells, involves multilayered structures of semiconductors with different band gap energies, such as GaAs, GaInP, InGaAs, GaInNAs and Ge, which result in efficiencies around 43%, however,

*e-mail: rrgoncalves@ffclrp.usp.br

until now, the high prices limit their use.⁸ All-organic PV and dye-sensitized solar cells, have been also described in the literature with efficiencies around 8.6-12.3%, exhibiting also high cost of manufacturing compared to Si-cells. Besides the relatively low PV cell efficiencies, the sunlight is diffused requiring large mirrors to concentrating it, which generates other drawbacks like the cost increase, and no shadowing regions to place these mirrors.⁸

Luminescent solar concentrators (LSC) arose as an interesting and groundbreaking strategy to improve photovoltaic energy conversion. The LSC consists of a film containing active optical centers, which after exposition to the sunlight absorb incident radiation and emit into a specific wavelength. Even part of the emission is lost at the surface, it can be redirected to a PV cell located in the edges of the film by total internal reflection, concentrating the light energy. In order to obtain an effective application, the optically centers in the film have some requirements such as a broad spectral absorption, high absorption efficiency over the absorption whole spectrum, high luminescence efficiency and large Stokes shift, emission compatibility with the PV-cell responsivity.⁸ In this sense, rare earth doped materials have been studied aiming LSC application. Recently, two main strategies have been described in the literature to improve the Si solar cell efficiency combining rare earth doped materials as energy converter. The first one is based on the use of materials which exhibit downconversion. Downconversion comprises the conversion of high energy photon (near-UV to visible range) into two or more low energy photons (near infrared). And the second strategy is combining the solar cell with materials which show upconversion process. The upconversion mechanism is based on the absorption of two or more low energy photons and emission of a high energy photon.^{24,25} One example for solar cell application is the absorption of two or more photons at NIR (1.5 μm) resulting in photon in the visible-NIR region (800-1000 nm).

It is known that the photophysical properties of rare earth ions are sensitive to the chemical environment and, therefore, the choice of host material is crucial. In the literature, most reports concerning NIR emission from Pr³⁺/Yb³⁺ co-doped materials are based on host with low phonon energy as fluoride and tellurite glasses resulting in interesting energy transfer mechanisms.^{11,17-19,26} In this work, a nanostructured oxide system was used as host, more precisely niobium oxide nanocrystals embedded in a silica based host.

Niobium oxide (Nb₂O₅) presents interesting optical properties, such as transparency over a wide range of wavelengths, low cut-off phonon energy (ca. 900 cm⁻¹)

and high refractive index (n = 2.4).²⁷ In addition, niobium oxide is polymorphic material and exhibits different crystalline phases depending on the annealing temperature and preparation method. Incorporating Nb₂O₅ nanocrystals in the SiO₂ matrix with controlled distribution of the rare earth ions in a low phonon energy environment, allowed an unusual achievement, the use of a silicate host to obtain an intense NIR emission. SiO₂ was applied as host due to its outstanding properties concerning photonic applications as waveguide, which brings potential applications as planar waveguides and solar concentrators. The addition of niobium oxide to the silica host tailor the properties of the glass or glass ceramic system, as the refractive index, structural features, with size and distribution of crystalline nanoparticles depending on the niobium content. Recently, rare earth-doped SiO₂-Nb₂O₅ nanocomposites have been studied by some of us. Er³⁺-doped SiO₂-Nb₂O₅ waveguides and nanocomposites were deposited by sol gel route. The crack-free waveguides exhibited excellent optical properties like uniform refractive index across the surface, efficient light injection at 1538 nm, not to mention the 1.5 μm luminescence, arousing great potential application in erbium doped waveguide amplifier (EDWA) and WDM devices.²⁷ In a further study,²⁸ a systematic study on the structural and spectroscopic properties of Er³⁺-doped nanocomposites was reported. How the different Nb₂O₅ polymorphs formation affected the structure and luminescence properties of the materials was the main focus and it was concluded that orthorhombic crystalline phase (T-phase), obtained by annealing the nanocomposites at 900 and 1000 °C at 70:30 and 80:20 SiO₂:Nb₂O₅ molar ratios, were the best potential candidates for many photonic applications. The rare earth ions confined into niobium oxide-rich environment has given unique and unusual luminescent properties.

In this context, Pr³⁺/Yb³⁺ co-doped SiO₂-Nb₂O₅ nanocomposites are proposed as feasible alternative to produce LSC and integrate the silicon solar cells. Therefore, in the present work, we focused on the spectroscopic properties of Pr³⁺/Yb³⁺ co-doped SiO₂-Nb₂O₅ nanocomposites and waveguides prepared by the sol gel method. More specifically, we analyzed the influence of Pr³⁺/Yb³⁺ content in relation to the Nb₂O₅ structural changes as well as in the luminescence properties of the studied nanocomposite materials.

Experimental

The Pr³⁺/Yb³⁺ co-doped SiO₂-Nb₂O₅ nanocomposites were synthesized via sol-gel method. The ethanolic solutions with total concentration of Si + Nb equal

to 0.448 mol L⁻¹ were attained at Si/Nb molar ratio of 70:30. Niobium ethoxide (Aldrich, 99.95%) and tetraethylorthosilicate (TEOS) (Merck, 98%) were used as precursors. PrCl₃ and YbCl₃ were used as Pr³⁺ and Yb³⁺ ions precursors, which were prepared from the respective oxides (Pr₂O₃, Aldrich 99.9% and Yb₂O₃, Aldrich 99.9%) by dissolution in 0.1 mol L⁻¹ HCl aqueous solution. After the total dissolution, a careful drying of the solutions was performed with anhydrous ethanol addition, obtaining the stock solutions. This later step enables control of water and acid content. The Pr³⁺:Yb³⁺ ions concentration ratio were 0.3:1.2 mol%, 0.5:2 mol% and 1:4 mol% (with respect to the total concentration of Si + Nb), which will be labeled S1, S2 and S3 hereafter.

S1, S2 and S3 were obtained as followed: the sol 1 was obtained by mixing TEOS, anhydrous ethanol and HCl at a 50:1 TEOS:HCl volume ratio. In a separate container, sol 2 was prepared by mixing niobium ethoxide, 2-ethoxyethanol and the Pr³⁺ and Yb³⁺ ions at a 10:1 2-ethoxyethanol:niobium ethoxide volume ratio. Next, sol 1 and the sol 2 were mixed together and kept under stirring at room temperature for 30 min. Then, a HCl aqueous solution with concentration 0.27 mol L⁻¹ was added at 1:0.007 TEOS:HCl molar ratio. The solution was filtered through a 0.2 μm Millipore filter and left to stand for 16 h, for waveguides deposition. Planar waveguides were deposited onto silica on silicon (10 μm SiO₂-Si(100) p-type) substrate by the dip-coating technique, at a dipping rate of 30 mm min⁻¹. The waveguides corresponding to Pr³⁺:Yb³⁺ ions concentration ratio S1, S2 and S3 ratios will be labeled W1, W2 and W3 hereafter. Before further coating, each layer was annealed for 60 s at 900 °C, until 50 layers were achieved. Finally, the resulting solutions were maintained at room temperature for 60 days for the xerogels formations. After that, the xerogels were milled to powder and annealed with a heating rate of 1 °C min⁻¹ at 900 °C and 1100 °C for 10h.

The X-ray diffraction (XRD) analyses were carried out on a Siemens-Bruker D5005-AXS diffractometer, with CuKα radiation, graphite monochromator, λ = 1.5418 Å, at 0.02° s⁻¹, in the 5-80° 2θ range. The Fourier transform infrared (FTIR) spectra were recorded on a Bomem MB102 spectrometer in the 4000-400 cm⁻¹ range, with a 2 cm⁻¹ resolution, using KBr pellets mixed with the powder samples (KBr:powder ratio of around 100:1). The photoluminescence (PL) spectra in the visible-NIR (range) were registered from the powders on a spectrofluorometer Fluorolog 3 Horiba Jobin Yvon equipped with a 450 W ozone free Xenon lamp. A Hamamatsu 10330-75 TE cooled detector with a NIR-PMT module was used for the detection.

Results and Discussion

Structural properties

X-ray diffraction patterns of S1, S2 and S3 nanocomposites annealed at 900 and 1100 °C are shown in Figures 1a and 1b, respectively. A large background was observed for S1 and S2 nanocomposites annealed at 900 °C in Figure 1a, which corresponds to amorphous silica host, accordingly with the JCPDS Card number 029-0085. In addition, two broad peaks at 22° and 29° overlap the halo, indicating an initial Nb₂O₅ crystallization. As the lanthanides content rise, better defined peaks patterns appeared, which can be attributed to crystallization of orthorhombic Nb₂O₅ T-phase (JCPDS 01-071-0336), corroborating with previous studies on Er³⁺-doped SiO₂-Nb₂O₅ nanocomposites and waveguides annealed at the same temperature.^{27,28} Nb₂O₅ phase transformation was observed on the nanocomposites annealed at 1100 °C. For the S1 nanocomposite, most of the reflection peaks can be attributed to monoclinic Nb₂O₅, named M-phase and also known as β-phase (JCPDS 00-019-0862), however, additional intense reflection peaks corresponding to T-phase could still be observed for this annealing temperature. This observation corroborates with recent studies of Er³⁺/Yb³⁺ co-doped SiO₂-Nb₂O₅ nanocomposites in our group, where the higher amount of lanthanide ions, lead to T-phase stability at higher annealing temperature (1100 °C), occurring only partial phase transformation to the M-phase. In the present work, for S2 and S3 nanocomposites, this crystallization change became more evident and practically only T-phase reflection peaks were observed, because even higher concentrations were used (lanthanides total content of 2.5 and 5 mol%, in contrast to 1.5 mol% of previous works). These structural changes indicate the significant contribution of the Ln³⁺ ions in the nucleation and crystallization processes, probably as nucleation agent. As a consequence, the Ln³⁺ distribution would be preferentially in the Nb₂O₅ rich environment, corroborating with our previous studies.

The average crystallite size was calculated using the Scherrer equation considering the (001) plane of the orthorhombic crystalline phase and assumed a spherical shape, to estimate the crystallite size. The higher the thermal treatment temperature, the larger the crystallite size. All the samples annealed at 900 °C have nanometric sizes of 7.0 nm, in agreement with previous report considering similar nanocomposites doped with Er³⁺ ions. For the samples annealed at 1100 °C, the crystallite size range from 26 to 32 nm considering S1 and S3. Figure 2 displays the TEM images of samples S2 annealed at 900 °C (Figure 2a)

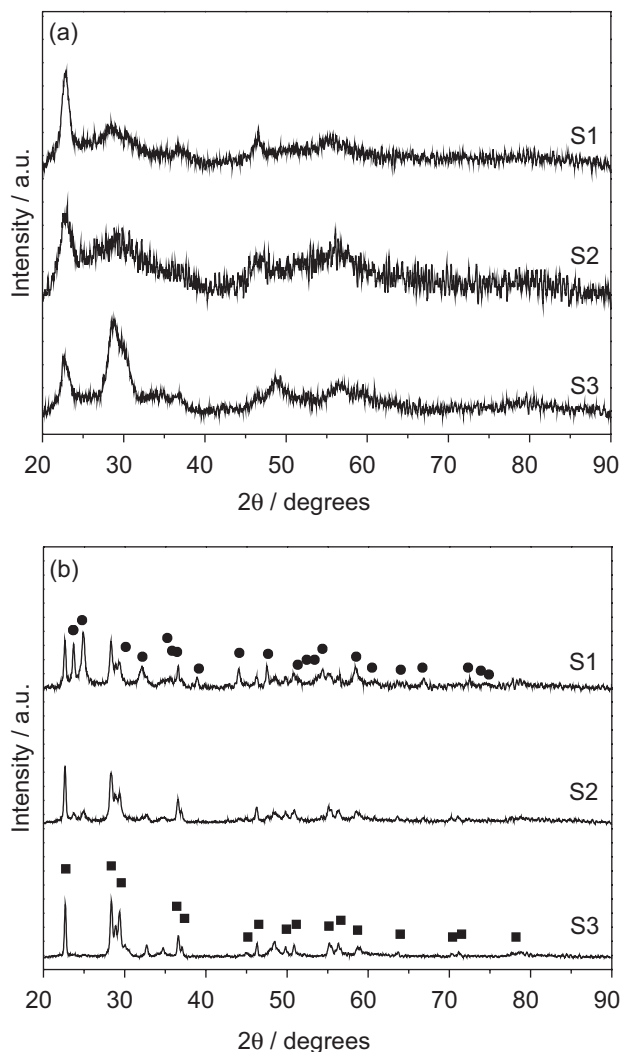


Figure 1. X ray diffractograms of the S1, S2 and S3 nanocomposites annealed at (a) 900 °C and (b) 1100 °C. The main reflection of T-phase (■) and M-phase (●) are depicted.

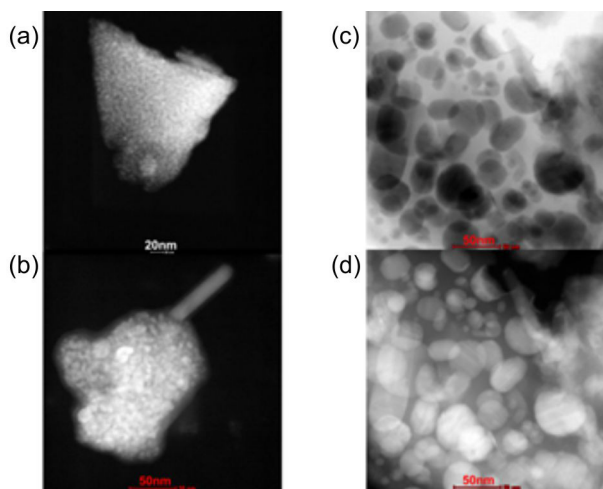


Figure 2. TEM images of samples (a) S2 annealed at 900 °C; (b) 0.3 mol% Er³⁺-doped SiO₂-Nb₂O₅ (70Si/30Nb molar ratio) annealed at 900 °C; (c) and (d) 0.3 mol% Er³⁺-doped SiO₂-Nb₂O₅ (70Si/30Nb molar ratio) annealed at 1100 °C.

and similar samples containing 0.3 mol% of Er³⁺ ions annealed at 900 °C (Figure 2b) and 1100 °C (Figures 2c and 2d). It can be seen a glass-ceramic formation with Nb₂O₅ nanoparticles dispersed in the amorphous SiO₂-based host occurs, in agreement with the XRD analysis. The particle size of the nanocrystals as well as the volume of the crystalline phase increase as the annealing temperature rise.

Figures 3a and 3b display the FTIR spectra of S1, S2 and S3, in the range of 4000 to 400 cm⁻¹ annealed at 900 and 1100 °C, respectively. The silica network can be confirmed by the vibrational modes at 1105, 811 and 466 cm⁻¹. The band around 466 cm⁻¹ observed for all the samples can be assigned to transverse-optical rocking motions (TO), perpendicular to the Si–O–Si plane of the oxygens bridging two adjacent Si atoms, while the band at 811 cm⁻¹ can be assigned to TO symmetric stretching of the O atom along a line bisecting the Si–O–Si bonds angle. The band located at 1105 cm⁻¹ can be assigned to the antisymmetric stretching of the oxygen atoms along a line parallel to Si–Si atoms axis, resulting in a transverse-optical mode (TO) antisymmetric stretching. This band is frequently accompanied by the shoulder at 1229 cm⁻¹ can be assigned to longitudinal mode (LO) of the same antisymmetric stretching or an admixture of TO and LO (longitudinal optical) components, which is more intense in porous materials.^{29–32} The band at 942 cm⁻¹ observed for the S1, S2 and S3 nanocomposites annealed at 900 °C (Figure 3a) can be attributed to Si–O–Nb and Si–OH stretching vibrations, indicating a binary system formation with covalent bond between SiO₂ and Nb₂O₅ as observed in a previous work.²⁸ Nevertheless, in the S1, S2 and S3 nanocomposites annealed at 1100 °C (Figure 3b), this band was not observed since OH elimination occurred. In addition, a band around 685 cm⁻¹ was observed for all the samples annealed at 900 and 1100 °C. Bands in the 740–580 cm⁻¹ can be assigned to Nb–O–Nb bridging stretching. As observed in a previous work, some Nb–O–Nb bands overlap with Si–O–Si bands at 800 and 450 cm⁻¹.²⁸

Photoluminescence spectroscopy

Figures 4a and 4b show the PL excitation spectra of S1, S2 and S3 nanocomposites monitoring the emission at 980 nm annealed at 900 and 1100 °C, respectively. In Figure 3a, a broad band with maximum at 324 nm can be observed and it is attributed to the SiO₂-Nb₂O₅ host absorption. In a previous work,²⁷ some of us have obtained a band gap energy value of 3.65 eV on Er³⁺-doped 70SiO₂-30Nb₂O₅ waveguides, which corresponds to the range of the observed broad band. Also, four bands can be observed with maxima at 445, 469, 485 and 589 nm,

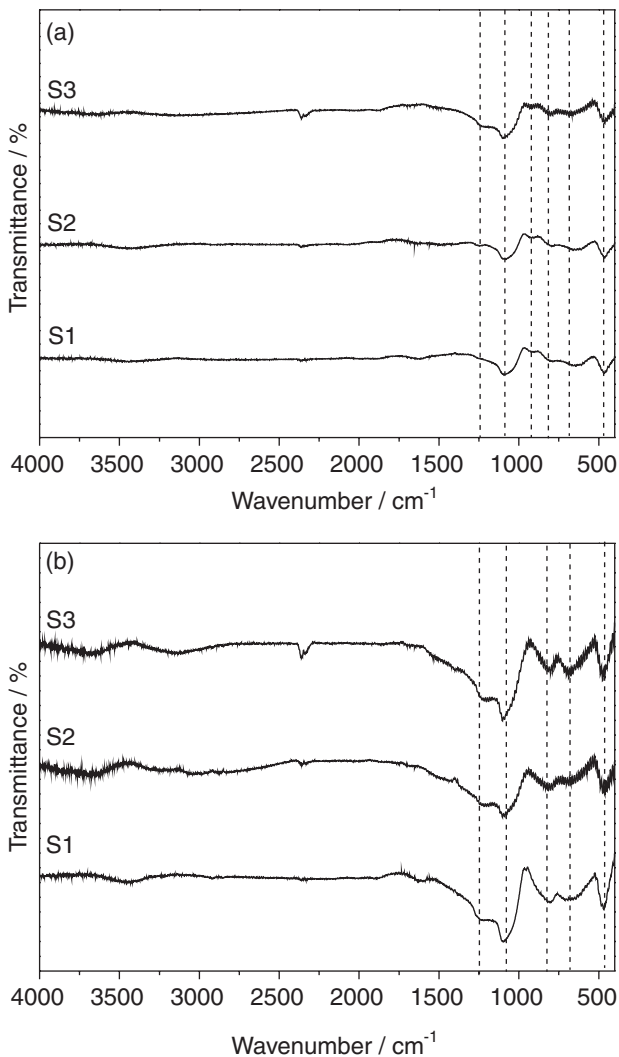


Figure 3. FTIR spectra of the S1, S2 and S3 nanocomposites annealed at (a) 900 °C and (b) 1100 °C.

which can be assigned to $^3H_4 \rightarrow ^3P_2$, $^3H_4 \rightarrow ^3P_1$, $^3H_4 \rightarrow ^3P_0$ and $^3H_4 \rightarrow ^1D_2$ transitions of Pr^{3+} ions, respectively. The observation of these Pr^{3+} excitation bands monitoring the emission corresponding to $^2F_{5/2} \rightarrow ^2F_{7/2}$ transition of Yb^{3+} ions, indicates an energy transfer process between Pr^{3+} and Yb^{3+} ions. The Pr^{3+} and Yb^{3+} ions transitions for S1, S2 and S3 nanocomposites annealed at 900 °C are shown in Figure 4c. The total intensity of the bands decreases as the rare earth content, probably due to quenching concentration.

In Figure 4b, a broad band with maxima at 374 nm was observed for the S1 nanocomposite, while for S2 and S3 lower intensities were observed for the same band. As discussed for the nanocomposites annealed at 900 °C, these bands correspond to $SiO_2-Nb_2O_5$ host absorption. Furthermore, the crystallization changes observed in the XRD analysis, reflected in the luminescence, i.e., increasing the lanthanide content it was observed a T-phase stability, while for S1 nanocomposite occurred a mixture of M and

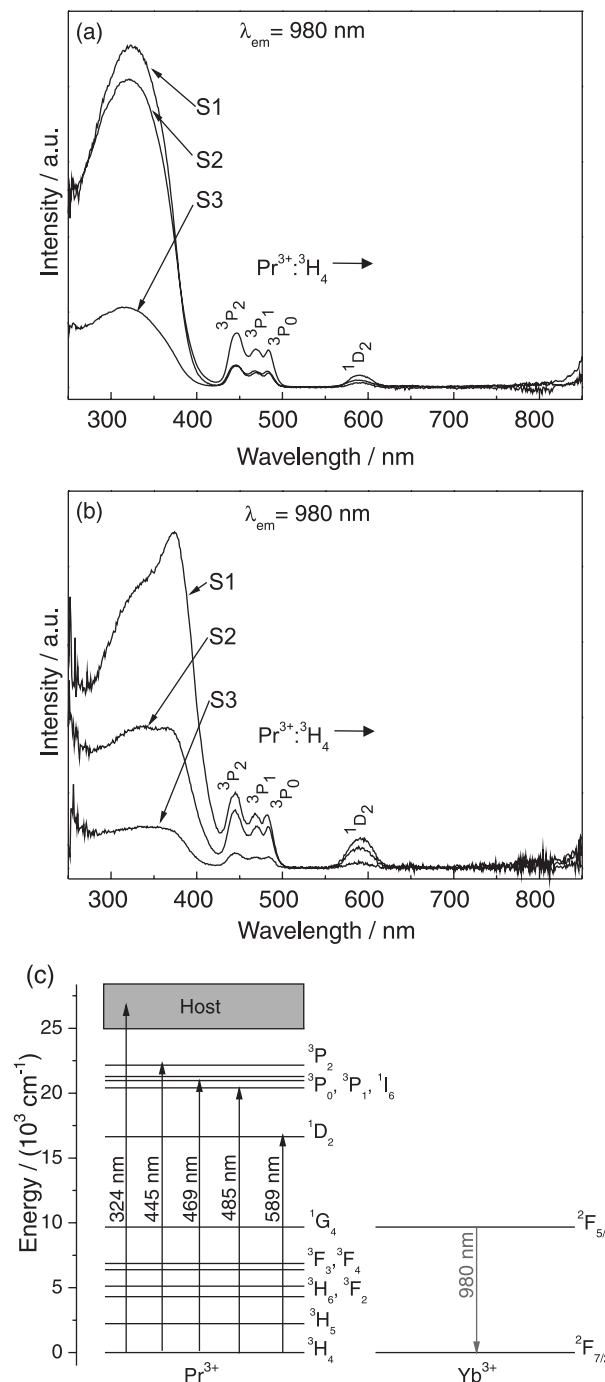


Figure 4. PL excitation spectra monitoring the 980 nm emission for S1, S2 and S3 nanocomposites annealed at (a) 900 °C; (b) 1100 °C. Pr^{3+} and Yb^{3+} transitions for nanocomposites annealed at 900 °C and 1100 °C are depicted in (c).

T-phases, which could explain the different profile observed for the same band at around 374 nm. Besides, bands with maxima at 444, 469, 482 and 589 nm were observed, which can be attributed to the Pr^{3+} transitions mentioned before, also evidencing an energy transfer process between Pr^{3+} and Yb^{3+} ions. The Pr^{3+} and Yb^{3+} ions transitions for S1, S2 and S3 nanocomposites annealed at 1100 °C are shown in Figure 4c.

Figures 5a and 5b show the emission spectra of S1, S2 and S3 nanocomposites annealed at 900 and 1100 °C under 300 nm excitation respectively, which corresponds to the SiO₂-Nb₂O₅ host absorption. In Figure 5a, there are emission bands with maxima centered at 592, 618, 650 and 703 nm, which can be assigned to the ¹D₂ → ³H₄, ³P₀ → ³H₆, ³P₀ → ³F₂, ³P₀ → ³F_{3,4} transitions of Pr³⁺ ions, respectively. Besides the aforementioned transitions of the Pr³⁺ ions, it can be observed a low-intensity band at 977 nm assigned to ²F_{5/2} → ²F_{7/2} transition of Yb³⁺ ions. Therefore, the observed emission bands indicate energy transfer from the host to Pr³⁺ and Yb³⁺ ions. The emission around 1000 nm will be discussed further in the text.

Figure 5b shows emission bands centered at 609 and 703 nm that can be assigned to ³P₀ → ³H₆, ³P₀ → ³F₃ transitions of Pr³⁺ ions. Comparing the nanocomposites annealed at 900 and 1100 °C, different relative intensities of the lanthanides transitions were observed, which can be

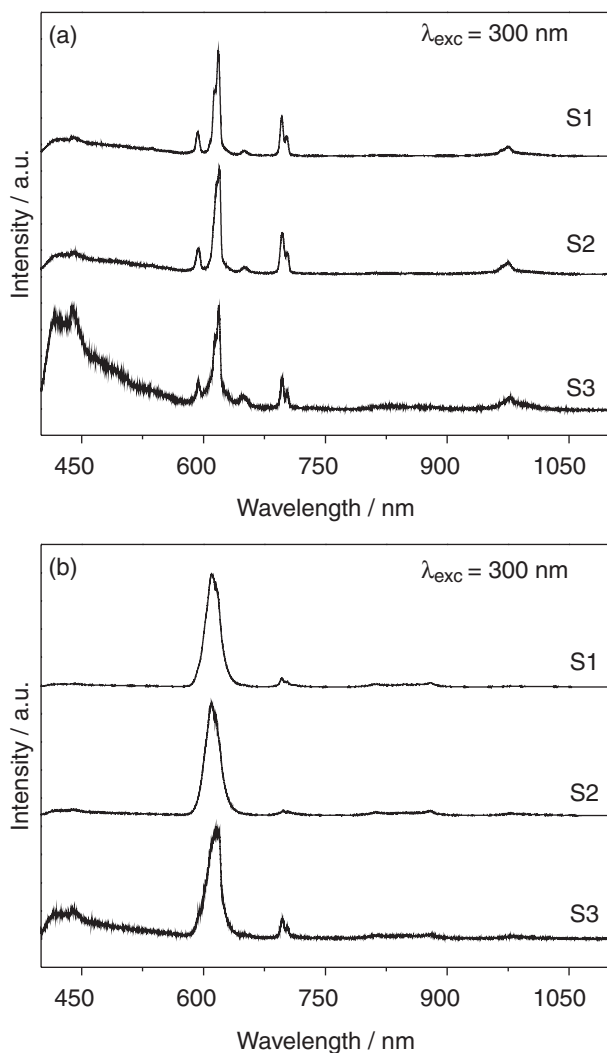


Figure 5. PL emission spectra of the S1, S2 and S3 nanocomposites upon excitation at 300 nm, annealed at: (a) 900 °C and (b) 1100 °C.

explained by the crystallization changes observed in XRD analysis, promoting a different lanthanides distribution in Nb₂O₅-rich sites.

Increasing the temperature, emission from the ¹D₂ was not observed, which will be an important feature to conclude about the mechanisms resulting in NIR emission.

The emission spectra of the S1, S2 and S3 nanocomposites annealed at 900 °C under 482 nm excitation is depicted in Figure 6a. Bands with maxima at 611, 646 and 732 nm can be ascribed to ³P₀ → ³H₆, ³P₀ → ³F₂ and ³P₀ → ³F₄, transitions of Pr³⁺ ions respectively. Moreover, the presence of the band at 974 nm assigned to ²F_{5/2} → ²F_{7/2} Yb³⁺ transition, under excitation at 482 nm, i.e., involving the excitation of the ³P₀ of Pr³⁺ energy level, attests energy transfer between Pr³⁺ to Yb³⁺ ions.^{20,33}

Figure 6b shows the S1, S2 and S3 nanocomposites annealed at 1100 °C under 482 nm excitation, where emission bands at 610, 646, 714 e 742 nm were observed.

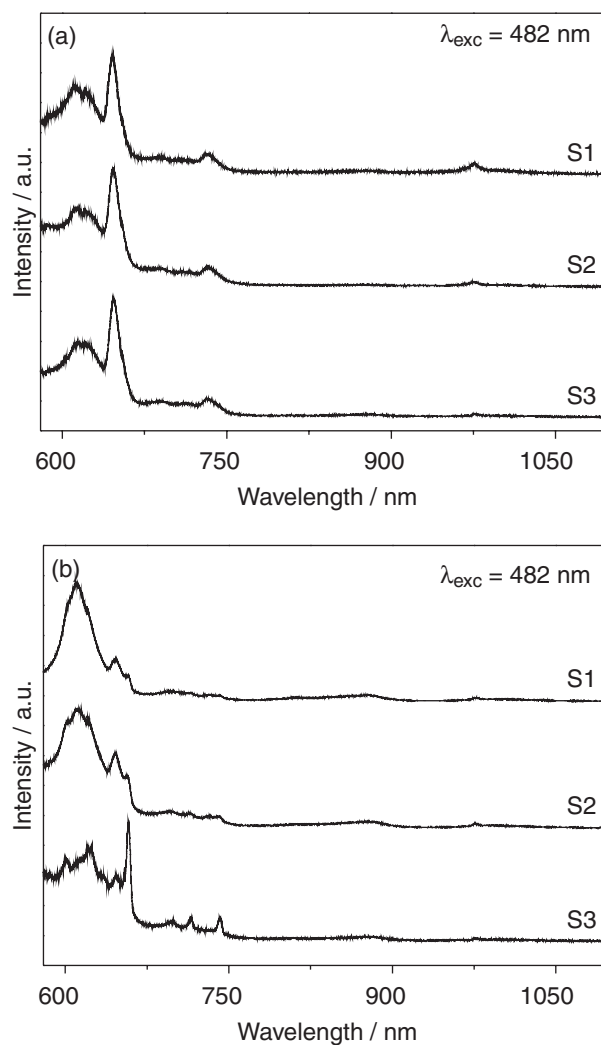


Figure 6. PL emission spectra of the S1, S2 and S3 nanocomposites upon excitation at 482 nm, annealed at: (a) 900 °C and (b) 1100 °C.

These bands are assigned to ${}^3P_0 \rightarrow {}^3H_6$, ${}^3P_0 \rightarrow {}^3F_2$, ${}^3P_0 \rightarrow {}^3F_3$ and ${}^3P_0 \rightarrow {}^3F_4$, respectively. Well resolved Stark components were observed in comparison with the nanocomposites annealed at 900 °C, which can be explained by the host structural changes.

Figure 7a shows the emission spectra of S1, S2 and S3 annealed at 900 °C in NIR range upon excitation at 350 nm, which corresponds to the $\text{SiO}_2\text{-Nb}_2\text{O}_5$ band gap energy. High-intensity emission bands at 980 nm with a shoulder at 1017 nm were observed, which can be attributed to ${}^2F_{5/2} \rightarrow {}^2F_{7/2}$ transition of Yb^{3+} ions,^{18,33} denoting an energy transfer from the host to Yb^{3+} ions. A drastic luminescence quenching was observed increasing the rare earth content, due to non-radiative processes. Increasing to 5 mol%, the rare earth ion-ion distance decreases, as a consequence energy migrations take place, which combined with host defects give rise to non-radiative decay and luminescence quenching.

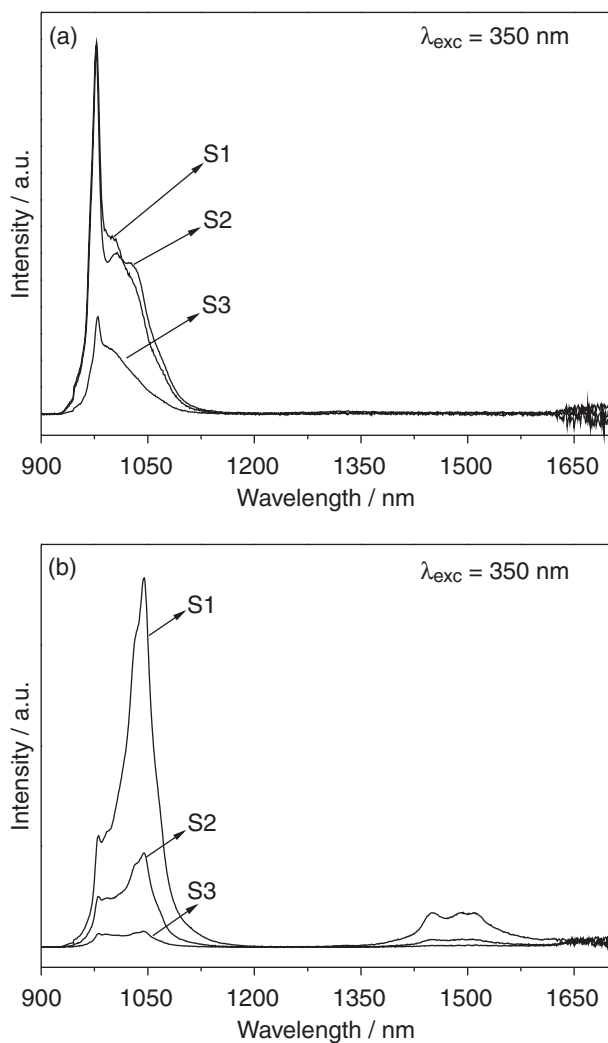


Figure 7. PL emission spectra of S1, S2 and S3 nanocomposites annealed at (a) 900 °C and (b) 1100 °C in the 900-1700 nm upon excitation at 350 nm.

The emission spectra of S1, S2 and S3 annealed at 1100 °C in NIR range upon excitation at 350 nm are presented in Figure 7b. A different spectral shape was observed, with higher intensity band at 1047 nm. The band at 979 nm can be assigned to the ${}^2F_{5/2} \rightarrow {}^2F_{7/2}$ transition of Yb^{3+} ions while the band at 1047 nm was attributed by some authors to the reabsorption of Yb^{3+} ions.^{18,34} In the literature, this last band is also attributed to the ${}^1D_2 \rightarrow {}^3F_3$ and ${}^1D_2 \rightarrow {}^3F_4$ transitions of Pr^{3+} ions.³⁵ Another band at 1449 nm attributed to the ${}^1D_2 \rightarrow {}^1G_4$ transition of Pr^{3+} ions was observed for the spectra of the samples annealed at 1100 °C. The presence of emission at 1449 nm indicates the 1D_2 population, strongly suggesting that the band at 1047 nm is attributed to the ${}^1D_2 \rightarrow {}^3F_3$ and ${}^1D_2 \rightarrow {}^3F_4$ transitions of Pr^{3+} ions.

The 1D_2 level population increases with the lanthanide concentration and annealing temperature, which can be explained by the presence of multiphonon relaxation and/or cross relaxation processes between Pr^{3+} ions (${}^3P_0 + {}^3H_4 \rightarrow {}^3H_6 + {}^1D_2$). Figure 8 shows the level diagrams of Pr^{3+} and Yb^{3+} ions evidencing the most important transitions and non-radiative processes observed for the samples annealed at 900 and 1100 °C, Figures 8a and 8b,

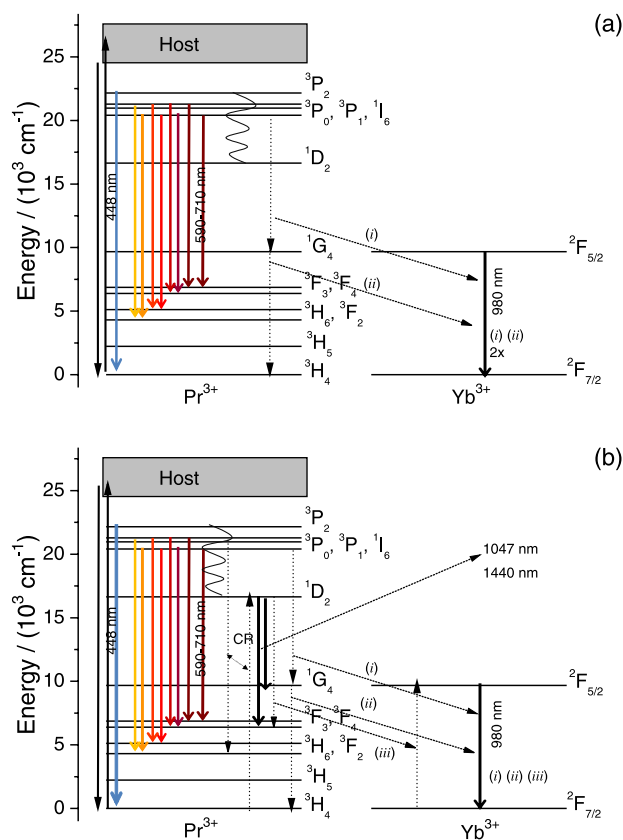


Figure 8. Partial Pr^{3+} and Yb^{3+} energy levels diagram. The radiative and non-radiative processes observed with excitation at 350 nm for nanocomposites annealed at 900 °C (a) and 1100 °C (b) are depicted.

respectively. Since the phonon energy doesn't significant change with annealing, it can be proposed that an efficient cross relaxation is the dominant process to populate the ¹D₂. Therefore, as the annealing temperature and Pr³⁺ content increases, the ion-ion interaction rises and the cross relaxation process become more efficient.

Figure 9a shows the emission spectra of S1, S2 and S3 nanocomposites annealed at 900 °C upon excitation at 448 nm. This wavelength corresponds to ³H₄ → ³P₂ transition of Pr³⁺ ions observed at the excitation spectra in Figure 3. The emission band at 980 nm with the shoulder at 1032 nm was observed, which can be attributed to the already discussed ²F_{5/2} → ²F_{7/2} emission of Yb³⁺ ions. Energy transfer process can be proposed between Pr³⁺ and Yb³⁺ neighboring ions. One possible mechanism can be the cooperative energy transfer between Pr³⁺ and Yb³⁺, which includes the excitation of Pr³⁺ ions from the ground state ³H₄ to the excited state ³P₂ at 448 nm with subsequent energy transfer for two neighboring Yb³⁺ acceptors which are excited from the ground state ²F_{7/2} to the ²F_{5/2} state and then emit at 980 nm. As a result, one photon in the visible range (at 448 nm) is converted into two NIR photons (at about 980 nm) in a single step energy transfer.^{18,34-36} The resonant two steps energy transfer is another downconversion process in which a part of the energy correlated with ³H₄ → ³P₀ is transferred to one ion Yb³⁺ neighbor ion through cross relaxation [Pr³⁺ (³P₀ → ¹G₄); Yb³⁺ (²F_{7/2} → ²F_{5/2})] (i) and then a second energy transfer takes place from the ¹G₄ intermediated level of the Pr³⁺ ions to the Yb³⁺ neighboring ions [Pr³⁺ (¹G₄ → ³H₄); Yb³⁺ (²F_{7/2} → ²F_{5/2})] (ii).^{36,37} Any excitation involving the ¹G₄ level was detected monitoring the emission at 980 nm. However, an additional band at 1300 nm was observed in Figure 8a, which can be attributed to ¹G₄ → ³H₅ of Pr³⁺ ions, indicating that the ¹G₄ level is populated and can contribute to NIR emission around 1000 nm.

It is well known that the Yb³⁺ ions have only two manifolds ²F_{7/2} and ²F_{5/2} and each of these manifolds has a maximum of four and three sublevels and, thereby, the shoulder at 1032 nm can be explained by the emissions of different sublevels. Dai *et al.*³⁸ have studied this so called radiative trapping effect on Yb³⁺-doped phosphate glasses. Radiative trapping can be described as a process in which photons that are spontaneously emitted from the metastable level are trapped by reabsorption by ions in the ground state. The excited state ions then relax by spontaneously emitting more photons, which are then reabsorbed, and the entire process is repeated. The authors have observed a shoulder around 1020 nm due to this effect even at low concentrations of Yb³⁺ ions, which became broader and more intense increasing this concentration. Increasing the rare earth content, it was observed another contribution to

the shoulder (1020 and 1040 nm), and the relative intensity between the emission at 1040 and 979 changes. The band at 1040 nm is attributed to the ¹D₂ → ³F₃ and ¹D₂ → ³F₄ transitions of Pr³⁺ ions.

Figure 9b presents the emission spectra of S1, S2 and S3 nanocomposites annealed at 1100 °C upon excitation at 448 nm. A higher intensity band 1041 nm in comparison to 979 nm was observed in the spectra, which can be attributed prominently to the ¹D₂ → ³F₃ and ¹D₂ → ³F₄ transitions of Pr³⁺ ions. In addition, the luminescence quenching by the rare earth increased content was observed for the spectra of the Figure 9b. Another band at 1449 nm attributed to the ¹D₂ → ¹G₄ transition of Pr³⁺ ions was observed for the spectra of the samples annealed at 1100 °C. As explained before, the ¹D₂ level population increases as the rare earth concentration and annealing temperature, which can be explained by multiphonon relaxation process or cross relaxation between Pr³⁺ ions (³P₀ + ³H₄ → ³H₆ + ¹D₂), as depicted in Figure 10.

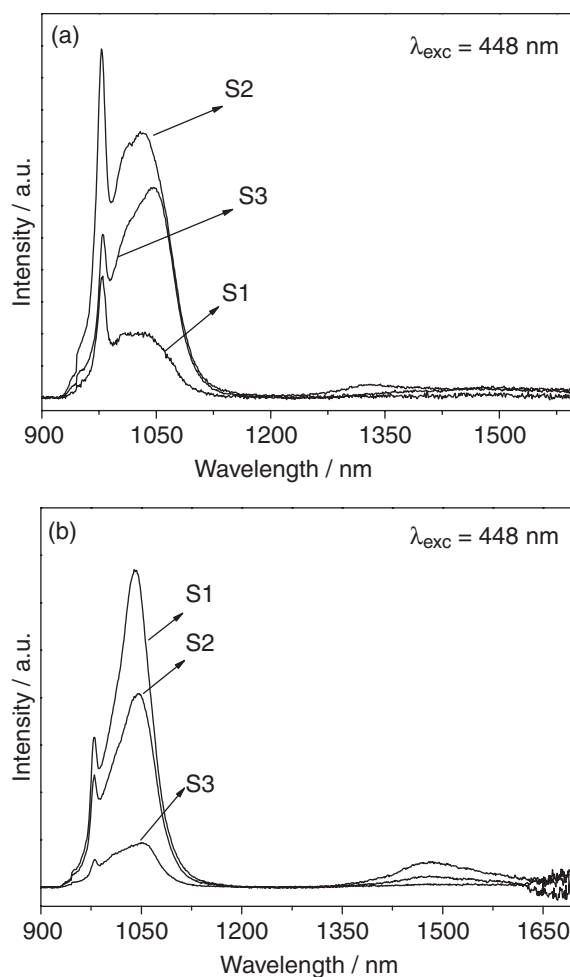


Figure 9. PL emission spectra of S1, S2 and S3 nanocomposites annealed at (a) 900 °C and (b) 1100 °C, in the 900-1700 nm upon excitation at 448 nm.

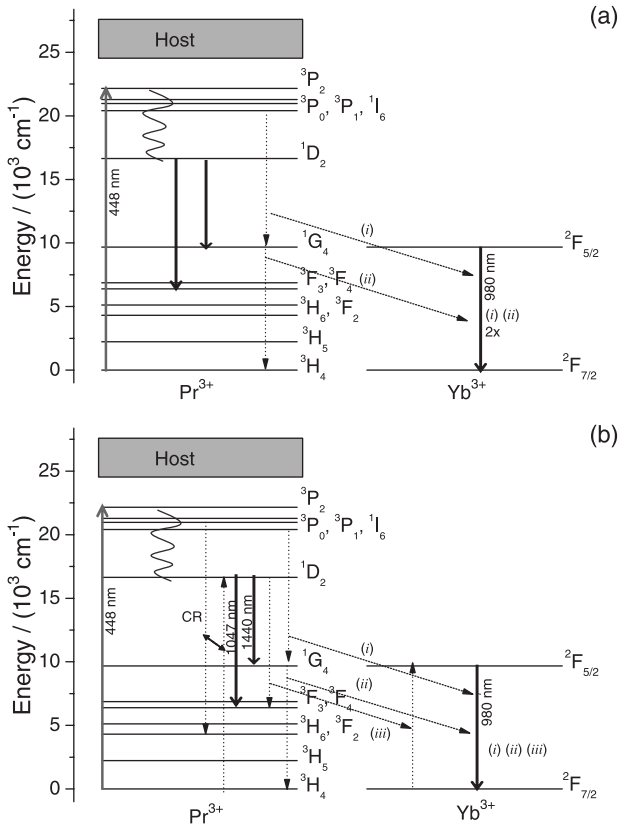


Figure 10. Partial Pr³⁺ and Yb³⁺ energy levels diagram. The radiative and non-radiative processes observed with excitation at 448 nm for nanocomposites annealed at 900 °C (a) and 1100 °C (b) are depicted.

Planar waveguides: optical characterization

Crack free waveguides were obtained. The optical parameters of the planar waveguides W1, W2 and W3 are reported in Table 1. The refractive index values and the number of propagation modes were similar to previous work on 0.3 mol% Er³⁺-doped SiO₂-Nb₂O₅ indicating the rare earth higher concentration did not affect the optical parameters.

The refractive index profiles of the W1, W2 and W3 waveguides reconstructed from the effective indices at 632.8 nm by an inverse Wentzel-Kramers-Brillouin method³⁹ are shown in Figure 11. The waveguides displayed a single step profile, with uniform refractive index across the thickness, corroborating for the high homogeneity of the films. Also, the similar profiles in the TE and TM modes revealed that birefringence was negligible.

Table 1. Optical parameters for W1, W2 and W3 waveguides at 632.8 nm

Parameter/Waveguide	W1 (TE/TM)	W2 (TE/TM)	W3 (TE/TM)
Number of modes at 632.8 nm	4/4	4/4	4/4
Refractive index at 632.8 nm	1.6740/1.6647	1.6815/1.6833	1.6830/1.6809
Film thickness / μm	1.60	1.64	1.63

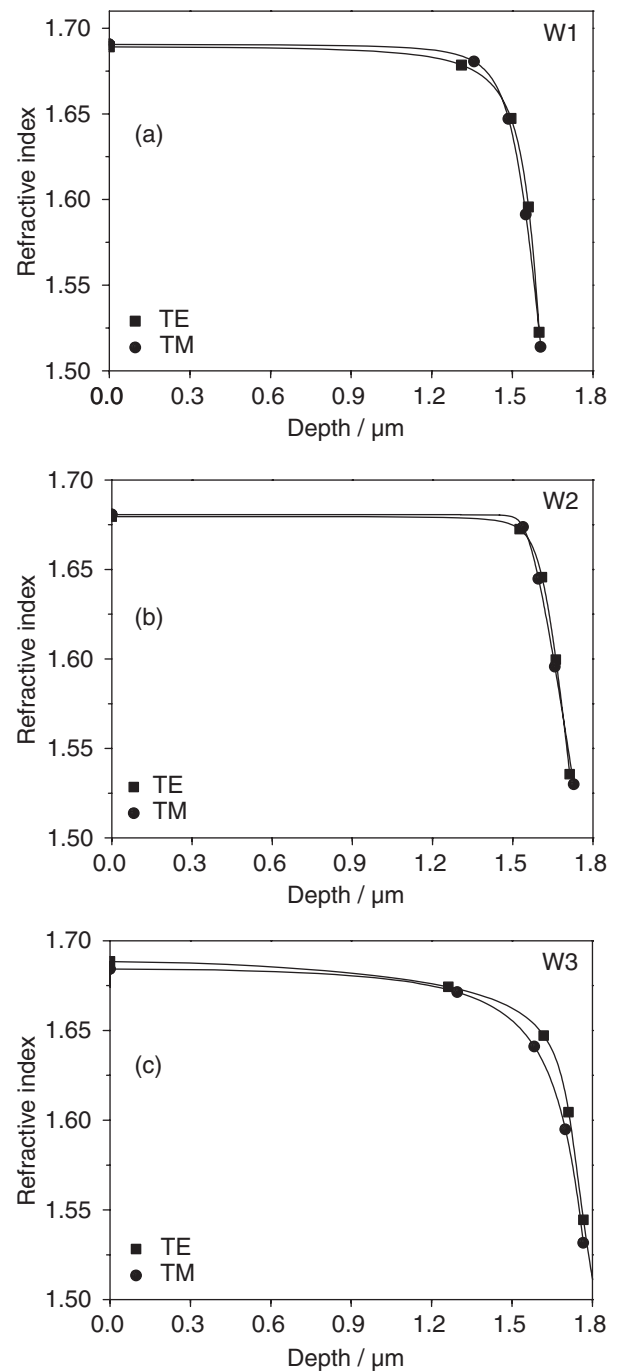


Figure 11. Refractive index profiles of the planar waveguides: (a) W1; (b) W2 and (c) W3, as reconstructed from modal measurements at 632.8 nm for TE and TM polarization. The effective refractive indices of the TE (■) and TM (●) are reported.

Figures 12a, 12b and 12c depict the squared electric field profiles for the TE₀ and TM₀ modes of the waveguides W1, W2 and W3 at 632.8 nm. The profiles were calculated by using the refractive index, thickness, propagation angles, and effective refractive index. The confinement coefficients

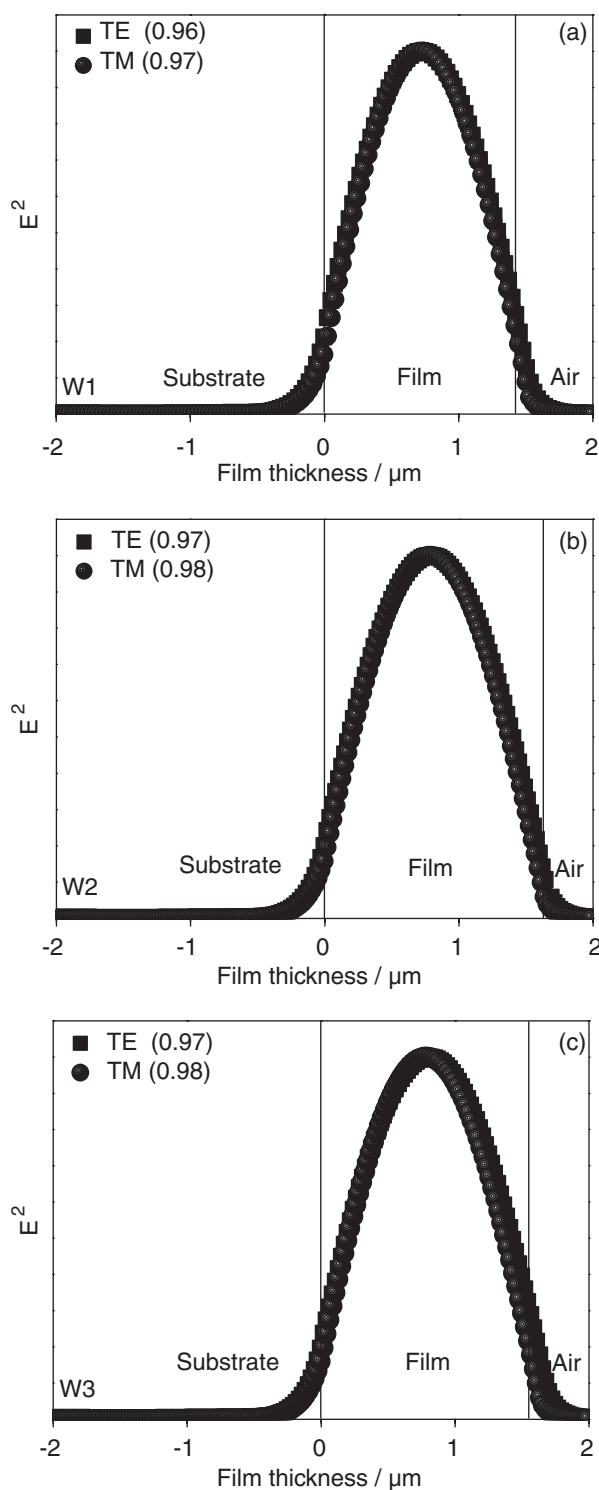


Figure 12. Calculated squared electric field profiles in the TE₀ and TM₀ mode at 632.8 nm for the (a) W1; (b) W2 and (c) W3 waveguides. The confinement coefficients are represented between parentheses.

were calculated using the integrated intensity ratio, i.e., the ratio between the field intensity in the guiding film and the total intensity, which also includes the squared evanescent field. All the values were equal or higher than 0.96 indicating efficient light injection at 632.8 nm.

Conclusions

In summary, the Pr³⁺/Yb³⁺ co-doped SiO₂-Nb₂O₅ nanocomposites and waveguides with Si/Nb molar ratio of 70:30 were obtained. Excitation and emission spectra have been recorded for all the samples in order to investigate the influence of rare earth concentration and differences of Nb₂O₅ crystallization of the samples annealed at 900 and 1100 °C.

Differences of luminescence profiles were observed for the sample depending on the excitation wavelength, annealing temperature and rare earth concentration. The excitation spectra monitoring the 980 nm emission revealed the energy transfer between the Pr³⁺ and Yb³⁺ ions. The energy transfer between Pr³⁺ to Yb³⁺ ions was observed upon excitation of ³P₂ level of Pr³⁺ ions at 448 nm. A higher intensity band at 1041 nm, ¹D₂ → ³F₃ and ¹D₂ → ³F₄ transitions of Pr³⁺ ions, in comparison to the band at 979 nm attributed to the ²F_{5/2} → ²F_{7/2} emission of Yb³⁺ ions was observed in the spectra of the samples with higher lanthanide concentrations and heated at higher temperatures. This fact together with the appearance of another band at 1449 nm attributed to the ¹D₂ → ¹G₄ transition of Pr³⁺ ions, indicates clearly the ¹D₂ level population increase as the lanthanide concentration and annealing temperature, which can be explained by multiphonon relaxation process or cross relaxation between Pr³⁺ ions (³P₀ + ³H₄ → ³H₆ + ¹D₂).

Waveguides with the same composition of the xerogels were obtained by dip-coating technique. The refractive indices and thicknesses of the films were measured by M-line technique. The films displayed a single step profile, with uniform refractive index across the thickness, indicating the high homogeneity of the films which makes them excellent candidates for solar concentrators.

As a general conclusion, the nanostructured Pr³⁺/Yb³⁺ co-doped SiO₂-Nb₂O₅ nanocomposites and waveguides show interesting NIR emission and optical properties for photonic applications, especially as energy converter for improving the efficiency of solar cells, by means of the UV and visible absorptions for NIR photons generation.

Acknowledgements

The authors acknowledge FAPESP (Brazil) and CNPq (Brazil) for financial support, CAPES for the scholarship.

References

1. da Silva Jr, C. M.; Bueno, L. A.; Gouveia-Neto, A. S.; *J. Non-Cryst. Solids* **2015**, *410*, 151.
2. del-Castillo, J.; Yanes, A. C.; Santana-Alonso, A.; Méndez-Ramos, J.; *Opt. Mater.* **2014**, *37*, 511.
3. Liu, Q.; Feng, W.; Li, F.; *Coord. Chem. Rev.* **2014**, *273-274*, 100.
4. Chatterjee, K.; Sarkar, S.; Jagajjani Rao, K.; Paria, S.; *Adv. Colloid Interface Sci.* **2014**, *209*, 8.
5. Wang, X.; Chang, H.; Xie, J.; Zhao, B.; Liu, B.; Xu, S.; Pei, W.; Ren, N.; Huang, L.; Huang, W.; *Coord. Chem. Rev.* **2014**, *273-274*, 201.
6. Boetti, N. G.; Lousteau, J.; Chiasera, A.; Ferrari, M.; Mura, E.; Scarpignato, G. C.; Abrate, S.; Milanese, D.; *J. Lumin.* **2012**, *132*, 1265.
7. Ferrari, J. L.; Lima, K. O.; Maia, L. J. Q.; Ribeiro, S. J. L.; Gonçalves, R. R.; *J. Am. Ceram. Soc.* **2011**, *94*, 1230.
8. Correia, S. F. H.; de Zea Bermudez, V.; Ribeiro, S. J. L.; Andre, P. S.; Ferreira, R. A. S.; Carlos, L. D.; *J. Mater. Chem. A* **2014**, *2*, 5580.
9. Bünzli, J.-C. G.; Chauvin, A.-S. In *Handbook on the Physics and Chemistry of Rare Earths*; vol. 44, 1st ed.; Gschneidner, K. A.; Bünzli, J.-C. G.; Vitalij, K. P., eds.; North-Holland: Amsterdam, Netherlands, 2014.
10. Tanabe, S.; Kouda, T.; Hanada, T.; *J. Non-Cryst. Solids* **2000**, *274*, 55.
11. Belançon, M. P.; Marconi, J. D.; Ando, M. F.; Barbosa, L. C.; *Opt. Mater.* **2014**, *36*, 1020.
12. Rolli, R.; Ronchin, S.; Montagna, M.; Moser, E.; Duverger, C.; Tikhomirov, V. K.; Jha, A.; Ferrari, M.; *J. Non-Cryst. Solids* **2001**, *280*, 269.
13. Manzani, D.; Pabœuf, D.; Ribeiro, S. J. L.; Goldner, P.; Bretenaker, F.; *Opt. Mater.* **2013**, *35*, 383.
14. Venkateswarlu, M.; Prasad, M. V. V. K. S.; Swapna, K.; Mahamuda, S.; Rao, A. S.; Babu, A. M.; Haranath, D.; *Ceram. Int.* **2014**, *40*, 6261.
15. Hölsä, J.; Laamanen, T.; Laihin, T.; Lastusaari, M.; Pihlgren, L.; Rodrigues, L. C. V.; *Opt. Mater.* **2014**, *36*, 1627.
16. Park, H.-A.; Lee, Y. K.; Im, W. B.; Heo, J.; Chung, W. J.; *Opt. Mater.* **2015**, *41*, 67.
17. Borrero-González, L. J.; Galleani, G.; Manzani, D.; Nunes, L. A. O.; Ribeiro, S. J. L.; *Opt. Mater.* **2013**, *35*, 2085.
18. Dieudonné, B.; Boulard, B.; Alombert-Goget, G.; Chiasera, A.; Gao, Y.; Kodjikian, S.; Ferrari, M.; *J. Non-Cryst. Solids* **2013**, *377*, 105.
19. Maalej, O.; Boulard, B.; Dieudonné, B.; Ferrari, M.; Dammak, M.; *J. Lumin.* **2015**, *161*, 198.
20. Serrano, D.; Braud, A.; Doualan, J. L.; Bolaños, W.; Moncorgé, R.; Camy, P.; *Phys. Rev. B* **2013**, *88*, 205144.
21. de Wild, J.; Meijerink, A.; Rath, J. K.; van Sark, W. G. J. H. M.; Schropp, R. E. I.; *Energy Environ. Sci.* **2011**, *4*, 4835.
22. Shalav, A.; Richards, B. S.; Green, M. A.; *Sol. Energy Mater. Sol. Cells* **2007**, *91*, 829.
23. Shockley, W.; Queisser, H. J.; *J. Appl. Phys.* **1961**, *32*, 510.
24. François, A.; *Chem. Rev.* **2004**, *104*, 139.
25. van der Ende, B. M.; Aarts, L.; Meijerink, A.; *Phys. Chem. Chem. Phys.* **2009**, *11*, 11081.
26. Damas, P.; Coelho, J.; Hungerford, G.; Hussain, N. S.; *Mater. Res. Bull.* **2012**, *47*, 3489.
27. Aquino, F. T.; Ferrari, J. L.; Ribeiro, S. J. L.; Ferrier, A.; Goldner, P.; Gonçalves, R. R.; *Opt. Mater.* **2013**, *35*, 387.
28. Aquino, F. T.; Pereira, R. R.; Ferrari, J. L.; Ribeiro, S. J. L.; Ferrier, A.; Goldner, P.; Gonçalves, R. R.; *Mater. Chem. Phys.* **2014**, *147*, 751.
29. Almeida, R. M.; Guiton, T. A.; Pantano, C. G.; *J. Non-Cryst. Solids* **1990**, *121*, 193.
30. Almeida, R. M.; Pantano, C. G.; *J. Appl. Phys.* **1990**, *68*, 4225.
31. Innocenzi, P.; *J. Non-Cryst. Solids* **2003**, *316*, 309.
32. Aronne, A.; Marenna, E.; Califano, V.; Fanelli, E.; Pernice, P.; Trifuoggi, M.; Vergara, A.; *J. Sol-Gel Sci. Technol.* **2007**, *43*, 193.
33. Lakshminarayana, G.; Yang, H.; Ye, S.; Liu, Y.; Qiu, J.; *J. Mater. Res.* **2008**, *23*, 3090.
34. Serrano, D.; Braud, A.; Doualan, J.-L.; Camy, P.; Moncorgé, R.; *J. Opt. Soc. Am. B* **2011**, *28*, 1760.
35. Gao, G.; Wondraczek, L.; *Opt. Mater. Express* **2013**, *3*, 633.
36. van Wijngaarden, J. T.; Scheidelaar, S.; Vlugt, T. J. H.; Reid, M. F.; Meijerink, A.; *Phys. Rev. B* **2010**, *81*, 155112.
37. Deng, K.; Wei, X.; Wang, X.; Chen, Y.; Yin, M.; *Appl. Phys. B* **2011**, *102*, 555.
38. Dai, S.; Yang, J.; Wen, L.; Hu, L.; Jiang, Z.; *J. Lumin.* **2003**, *104*, 55.
39. Chiang, K.; *J. Lightwave Technol.* **1985**, *3*, 385.

Submitted: June 18, 2015

Published online: August 4, 2015

FAPESP has sponsored the publication of this article.